arXiv:1103.1915v1 [astro-ph.GA] 9 Mar 2011

Submillimeter and molecular views of three Galactic ring-like H II regions

K. Arvidsson

Astronomy Department, Adler Planetarium, 1300 South Lake Shore Drive, Chicago, IL 60605, USA; karvidsson@adlerplanetarium.org

C. R. Kerton

Department of Physics & Astronomy, Iowa State University, Ames, IA 50011, USA; kerton@iastate.edu

ABSTRACT

We use SCUBA 850 μm and CO observations to analyze the surroundings of three Galactic ring-like H II regions, KR 7, KR 81 and KR 120 (Sh 2-124, Sh 2-165 and Sh 2-187), with the aim of finding sites of triggered star formation. We find one prominent submillimeter (sub-mm) source for each region, located at the interface between the H II region and its neutral surroundings. Using Two Micron All Sky Survey photometry, we find that the prominent sub-mm source for KR 120 probably contains an embedded cluster of young stellar objects (YSOs), making it a likely site for triggered star formation. The KR 7 sub-mm source could possibly contain embedded YSOs, while the KR 81 sub-mm source likely does not. The mass column densities for these dominant sub-mm sources fall in the $\sim 0.1 - 0.6$ g cm^{-2} range. The mass of the cold, dense material (clumps) seen as the three dominant sub-mm sources fall around ~ 100 $M_{\odot}$. We use the SCUBA Legacy catalog to characterize the populations of sub-mm sources around the H II regions, and compare them to the sources found around a previously studied similar ring-like H II region (KR 140) and near a massive star-forming region (W3). Finally, we estimate the IR luminosities of the prominent newly detected sub-mm sources and find that they are correlated with the clump mass, consistent with a previously known luminosity-mass relationship which this study shows to be valid over four orders of magnitude in mass.

Subject headings: H II regions - ISM: bubbles - ISM: clouds - stars: formation - stars: massive - surveys

1. Introduction

Young stellar objects (YSOs) are often observed at the peripheries of H II regions, suggesting that star formation can be triggered at such locations (Elmegreen 1998; Deharveng et al. 2005). This study is aimed at investigating such sites of possible triggered star formation around a sample of ring-like H II regions. These H II regions have a distinctive ring morphology in *Midcourse Space Experiment* Galactic Plane Survey (*MSX*; Price et al. 2001) A-band ($\lambda_0 = 8.3$ μm, FWHM $\Delta\lambda = 7 - 11$ μm) images filled with radio continuum emission. *MSX* A-band emission is dominated by intense line emission from polycyclic aromatic hydrocarbons (PAHs) that arises in the interface between ionized gas in the H II region and the surrounding molecular material. Inside the H II region the flux of ultraviolet (UV) photons is sufficiently high to destroy PAHs. Outside of the PAH-free region, in the photodissociation regions, the less energetic UV photon flux excites PAHs but does not destroy them. Moving farther into the cooler molecular gas the UV flux decreases rapidly and PAHs are likely incorporated into larger dust grains. The result is a striking ring-like or "halo" morphology the PAH emission traces an interface region where new stars are possibly being formed.

This study means to address the following issues. What are the physical conditions such as mass and column density at the sites of possible star formation? How many such sites are there? What is the YSO content? This study will look at submillimeter (sub-mm) and molecular line observations toward a selected sample of three ring-like H II regions, KR 7 (Sh 2-124), KR 81 (Sh 2-165), and KR 120 (Sh 2-187) (Sharpless 1959; Kallas & Reich 1980). These single star powered regions were chosen to minimize the effects of feedback from multiple massive stars. They were selected based on their appearance in the Canadian Galactic Plane Survey (CGPS; Taylor et al. 2003) and *MSX*, displaying the expected roughly circular radio morphology, a ring-like infrared morphology, and a small angular size. Figures 1, 2 and 3 show *MSX* A-band images ($\sim 18''$ resolution) of the ring-like H II regions KR 7, KR 81, and KR 120, respectively, overlaid with 1420 MHz radio continuum contours ($\sim 1'$ resolution). For KR 120, the radio source seen at the edge of the main H II region contours is an extragalactic background source. Positions and various other designations of these H II regions are listed in Table 1.

In addition, these new data will be combined with data on KR 140, another small ring-like H II region that has been the subject of several studies (Kerton et al. 1999; Ballantyne et al. 2000; Kerton et al. 2001, 2008). This larger sample will be contrasted with sub-mm observations of a very different environment, the interface between the massive star-forming complex W3 and its surrounding molecular cloud.

2. Observations

2.1. Sub-mm observations

The sub-mm observations were obtained using the Submillimeter Common-User Bolometer Array (SCUBA) on the 15 m James Clerk Maxwell Telescope (JCMT) at Mauna Kea, Hawaii. SCUBA was used to acquire 450 μm and 850 μm images (at $\sim 8''$ and $\sim 15''$ resolution respectively) during 11 nights in 2003, August 12, 15, and 17, September 17 and 24-26, and October 4 and 9-11.

The reduction was performed following the SCUBA map reduction cookbook[1]. Standard commands within the SCUBA reduction package SURF were used to apply flat fields, correct for the signal attenuation in the atmosphere, remove spikes, remove base lines, identify noisy bolometers and remove sky noise. For the observations at 450 μm, the weather was too poor and no sources could be seen in the images. These 450 μm observations have been excluded from further study. The individual reduced 850 μm images were calibrated into Jy beam^{-1} using the primary calibration source Uranus. To account for the varying background, the reduced and calibrated images were smoothed to a resolution of $120''$. The smoothed images were then subtracted from the reduced and calibrated images, thus removing large-scale structure ($> 120''$). The background-subtracted images of the same target were then co-added to reduce the noise level. The resulting final background-subtracted images were then used in the subsequent analysis. They have noise levels of $0.07 - 0.04$ Jy beam^{-1}.

Figures 4, 10 and 16 show the final 850 μm images of KR 7, KR 81, and KR 120, respectively. By visual examination, they each have one prominent 850 μm source with a signal-to-noise ratio (S/N) greater than 6 that is located on the "rim" seen in the *MSX* images. Faint (S/N $\lesssim 4$) extended sub-mm emission can sometimes be seen that usually lines up with *MSX* emission.

The SCUBA Legacy Catalogues paper (Di Francesco et al. 2008) provides an archive of SCUBA observations, including ours, reduced using a different method (the "matrix inversion" method described in Johnstone et al. 2000). From these images, catalogs of sources have been extracted using an automated object identification program based on the CLUMPFIND algorithm. By cross-checking the results of the two different reduction techniques we are able to increase the number of detected sub-mm sources around the H II regions.

2.2. Molecular observations

Observations of CO ($J = 1 \rightarrow 0$) line emission from the isotopes ^{12}CO (115.3 GHz), ^{13}CO (110.2 GHz) and C^{18}O (109.8 GHz) were obtained using the SEcond QUabbin Optical Imaging Array (SEQUOIA) at the FCRAO 14 m telescope in Massachusetts. The reduction, calibration and processing of the raw data into science-ready data cubes was done by C. Brunt in 2004. The molecular line cubes have a spectral resolution of 0.25 km s^{-1} and an angular resolution of 46″. The flux scale uncertainty is taken to be $\sim$ 15% from Jackson et al. (2006), who used the same instrument to conduct the Galactic Ring Survey.

---

[1] http://docs.jach.hawaii.edu/star/sc11.htx/sc11.html

3. Analysis

3.1. KR 7

KR 7 (Sh 2-124) is a 12′ diameter H II region with a 1420 MHz flux density $F_{1420} = 2690 \pm 81$ mJy (Kerton 2006). Using a spherical, constant density model, a lower limit on the total emission rate of ionizing photons (N_L) can be derived from the observed radio flux density

$$N_L \geq 7.5 \times 10^{43} F_\nu d^2 \nu^{0.1} T_e^{-0.45} \text{ s}^{-1} \quad (1)$$

where ν is the frequency in GHz, F_ν is the flux density measured at frequency ν in mJy, d is the distance to the source in kpc, and T_e is the electron temperature in units of 10^4 K (Rudolph et al. 1996). The flux of ionizing photons, $\log N_L = 48.2$, corresponds to a O9 V star (Crowther 2005). Crampton et al. (1978) classify the possible exciting star of KR 7 (LS III +50°24) as a B0 V star. However, they note that it is not located in the brightest part of the nebula and Lahulla (1985) concludes that LS III +50°24 is too cool, leaving the identity of the exciting star for KR 7 an open question.

For KR 7, the final 850 μm image is shown in Figure 4, and the associated CO emission peaks around -43 km s^{-1} and is mainly found to the Galactic west (smaller Galactic longitude) of the H II region, see Figure 5. There is also a smaller CO concentration to the Galactic northeast of the H II region. The left panel of Figure 5 shows integrated ^{12}CO emission (integrated between $-47.5 < V_{\rm LSR} < -39.5$ km s^{-1}) and the right panel shows ^{13}CO (integrated between $-47.5 < V_{\rm LSR} < -42.8$ km s^{-1}) overlaid with *MSX* A-band contours corresponding to the feature seen in Figure 1. For this region and velocity range, C^{18}O barely shows a signal above the noise, even when integrated over a velocity range. C^{18}O analysis is thus not carried out for KR 7. The ^{12}CO and ^{13}CO emission exhibit peaks in the same locations, most notably in a small complex stretching from the location of the sub-mm source up toward the Galactic northwest. This can easily be seen in the lower right corner of Figure 6 that shows the 850 μm images overlaid with ^{13}CO contours. The peak integrated ^{13}CO emission ($I_{\rm peak}$) at the location of the sub-mm source has a value of 7.9 ± 1.2 K km s^{-1}, which corresponds to a ^{13}CO-based $N(\text{H}_2) = (5.7 \pm 0.9) \times 10^{21}$ cm^{-2} or $N(M) = 0.026 \pm 0.004$ g cm^{-2}. The ^{13}CO and C^{18}O (when available) column densities were calculated using the expression (Rohlfs & Wilson 2004, Equation (14.40))

$$N(\text{CO}) = 1.3 \times 10^{15} \int T_{\rm MB} \mathrm{d}V \text{ cm}^{-2} \quad (2)$$

for an assumed main beam temperature of 20 K. Using conversion factors from Simon et al. (2001) and references therein ($R(^{12}\text{CO}/^{13}\text{CO}) = 45$ and $R(^{12}\text{CO}/\text{H}_2) = 8 \times 10^{-5}$) the peak H$_2$ column density ($N(\text{H}_2)_{\rm peak}$) was calculated in cm^{-2}. The peak mass column density was obtained by multiplying $N(\text{H}_2)_{\rm peak}$ with the H$_2$ molecular mass and a factor of 1.36 to account for elements heavier than hydrogen (Simon et al. 2001). The uncertainties shown are due to noise in the maps and the $\sim$ 15% flux scale uncertainty. They do not include the dominant systematic uncertainty arising from various assumptions in the analysis method, and consequently the values calculated from CO data are expected to be lower limits and accurate within a factor of a few (Simon et al. 2001). To relate $N(\text{H}_2)$ and the integrated ^{12}CO emission, the conversion factor of $X = 2.3 \times 10^{20}$ cm^{-2} (K km $s^{-1})^{-1}$ was used (Rohlfs & Wilson 2004). By summing over the entire ^{12}CO feature seen in Figure 5, the mass of the molecular material surrounding KR 7 is estimated to be $\sim 3600\ M_\odot$.

The visually dominant KR 7 sub-mm source (JCMTSF J213822.5+501908; Di Francesco et al. 2008) has a flux density (F_{850}) of 1.1 ± 0.2 Jy within an aperture of 25″ around the peak. The deconvolved radius is $\sim$ 24″ and corresponds to a physical diameter of 0.6 pc at a distance of 2.8 kpc. The maximum brightness (B_{850}) is 0.5 Jy beam^{-1} (S/N $\sim$ 13). Using standard conversion factors for SCUBA 850 μm observations (4.60×10^{22} cm^{-2} (Jy beam$^{-1})^{-1}$ and 6.2 $M_\odot$ Jy^{-1} kpc^{-2} from Table A.1 in Kauffmann et al. 2008) together with an assumed dust temperature $T_d = 20$ K and a distance of 2.8 ± 0.4 kpc (Foster & Routledge 2003), B_{850} corresponds to a dust-derived peak column density of $N(\mathrm{H_2}) = (2.3 \pm 0.5) \times 10^{22}$ $\mathrm{cm^{-2}}$ or $N(M) = 0.11 \pm 0.02$ g $\mathrm{cm^{-2}}$. The dust-based column density is greater than the ^{13}CO-based column density for the same location. This could be a result of the ^{13}CO becoming optically thick in the densest regions. The mass of the sub-mm source is 51 ± 19 $M_\odot$, where the listed uncertainty is the combination of the uncertainty in distance and flux density. Dust-based column density and mass estimates are sensitive to the dust temperature. For example, if the dust temperature was instead assumed to be $T_d = 10$ K, the column density would increase to 6.7×10^{22} $\mathrm{cm^{-2}}$ or $N(M) = 0.31$ g $\mathrm{cm^{-2}}$ and the mass of the sub-mm core would increase to 150 $M_\odot$.

For KR 7, the SCUBA Legacy image corresponding to Figure 4 looks very similar, except for a bright part near the edge of the image to the Galactic northeast ($\ell = 94\overset{\circ}{.}55$, $b = -1\overset{\circ}{.}45$) that is absent in Figure 4. The SCUBA Legacy catalog contains several sources. The main source (JCMTSF J213822.5+501908) is the most prominent one in the catalog with S/N = 13, $B_{850} = 0.73 \pm 0.06$ Jy $\mathrm{beam^{-1}}$ and $F_{850} = 1.62$ Jy (absolute flux density uncertainty can be as large as 30%; see Di Francesco et al. 2008). The corresponding dust-derived peak column density is $N(\mathrm{H_2}) = (3.4 \pm 0.7) \times 10^{22}$ $\mathrm{cm^{-2}}$ or $N(M) = 0.16 \pm 0.03$ g $\mathrm{cm^{-2}}$ and the corresponding mass is 78 ± 32 $M_\odot$ which agrees, within the uncertainties, with our derived mass. The SCUBA Legacy catalog also identifies 10 other faint sources (S/N $\lesssim 4.4$) within and around the region indicated with ^{13}CO contours in the lower right corner of Figure 6. The corresponding locations of the sources have about the same S/N in our image (see Figure 4) but are harder to identify visually. These probable sources are listed in Table 3 together with the corresponding peak mass column densities and masses. In addition, the Legacy catalog lists 21 sources associated with the concentration of ^{13}CO near $\ell = 94\overset{\circ}{.}57$, $b = -1\overset{\circ}{.}45$. Inspection of the SCUBA Legacy image shows that these sources are all located in a bright noisy gradient near the edge of the image. We therefore believe most of these sources are spurious and, as we are unable to confidently identify those few sources that may be real, we do not consider any of these sources in further analysis.

The main KR 7 850 μm source is spatially associated with IRAS 21366+5005 and MSX6C G094.4674-01.5705. In the *IRAS* PSC, 12, 25, and 60 μm flux densities are listed as being good quality flux densities, while the 100 μm flux density only is an upper limit. In the *MSX6C* catalog, the source is not detected in the bands C (12.1 μm, $11.1 - 13.2$ μm) and E (21.3 μm, $18.2 - 25.1$ μm), but is detected in the bands A and D (14.7 μm, $13.5 - 15.9$ μm). Figure 7 shows the spectral energy distribution (SED) of this source from 8.3 to 850 μm. *IRAS* PSC values are squares, *MSX6C* PSC values are diamonds and the 850 μm cross is the 1.1 ± 0.2 Jy found in this work. The arrow indicates an upper limit. Note that in the logarithmic flux density scale, the 1σ uncertainty lines drawn often are smaller than the printed symbol. Integrating under the curve using the Emerson (1988) method for the *IRAS* fluxes yields an upper limit to the total integrated luminosity (L_{IR}) of ~ 500 $L_\odot$. The measured and calculated quantities are given in Table 2.

Figure 8 shows a composite image of the region ($\sim 1\overset{\prime}{.}6 \times 2'$) surrounding the dominant KR 7 850 μm source, made from Two Micron All Sky Survey (2MASS) *J*-band (Blue), *H*-band (Green) and K_s-band (Red) images. The contours, 850 μm brightness levels of 0.15, 0.3, and 0.45 Jy $\mathrm{beam^{-1}}$, trace the very central part of the sub-mm source. The 2MASS catalog lists seven sources within a radius of $\sim 0\overset{\prime}{.}25$ from the location of the peak B_{850}, an area roughly corresponding to the extent of the 850 μm 0.15 Jy $\mathrm{beam^{-1}}$ contour. Figure 9 shows these sources plotted in a 2MASS color-color diagram (top) and a color-magnitude diagram (bottom). The solid lines in the lower left corner of the color-color diagram show the intrinsic colors of main-sequence (V) and giant (III) stars (Koornneef 1983; Bessell & Brett 1988). The parallel lines show $A_V = 20$ reddening vectors for a K5 V and a O9 V star derived using the infrared extinction law of Rieke & Lebofsky (1985). For the color-magnitude diagram, the main-sequence and giant branch are shown with some representative spectral types at a distance of 2.8 kpc. The parallel lines are again $A_V = 20$ reddening vectors for a K5 V and a O9 V star. The size of the plotted crosses for the 2MASS sources in both diagrams indicates the uncertainty in 2MASS photometry. An arrow indicates sources where the 2MASS catalog only lists an upper brightness limit in the relevant band. The three sources near the main-sequence lines are probably foreground stars. The two sources labeled "1" and "2" in Figure 8 and Figure 9 have $H - K \geq 2$ and are probably highly embedded YSOs that would be associated with the cold dust core detected in the 850 μm image.

3.2. KR 81

KR 81 (Sh 2-165) is a 6′ diameter 1420 MHz radio continuum source with a flux density $F_{1420} = 607 \pm 40$ mJy (Kerton 2006). The estimated flux of ionizing photons, $\log N_L = 47.2$ corresponds to a single B0 V star (Crowther 2005). This agrees well with observations of the exciting star BD +61 2494, listed as a B0 V star in Crampton & Fisher (1974) or B0.5 V in Hunter & Massey (1990).

For KR 81, the final 850 μm image is shown in Figure 10, and the associated CO emission peaks around -34 km s^{-1} and is mainly found to the Galactic northwest (smaller Galactic longitude) of the H II region, where the prominent sub-mm source, discussed in the next paragraph, is located (see Figure 11). There is also CO to the Galactic southeast of the H II region. Figure 11 shows integrated CO emission from ^{12}CO (left panel, integrated between $-37.5 < V_{\rm LSR} < -29.4$ km s^{-1}) and ^{13}CO (right panel, integrated between $-35.5 < V_{\rm LSR} < -31.8$ km s^{-1}) overlaid with *MSX* A-band contours corresponding to the feature seen in Figure 2. The $I_{\rm peak}$ of the integrated ^{13}CO emission at the location of the sub-mm source has a value of 13.5 ± 2.0 K km s^{-1}, which corresponds to a ^{13}CO-based $N({\rm H_2}) = (9.8 \pm 1.5) \times 10^{21}$ cm^{-2} or $N(M) = 0.045 \pm 0.007$ g cm^{-2}. C^{18}O emission is detected toward this region (see Figure 12) and shows a strong peak at the location of the sub-mm source. Using the isotope number ratio R(C^{18}O/H$_2$) $= 1.7 \times 10^{-7}$ (Rohlfs & Wilson 2004), the C^{18}O-based column density is $N({\rm H_2}) = (1.0 \pm 0.2) \times 10^{22}$ cm^{-2} or $N(M) = 0.045 \pm 0.007$ g cm^{-2}, very close to the estimate from ^{13}CO. By summing over the entire ^{12}CO feature seen in Figure 11, the mass of the molecular material surrounding KR 81 is estimated to be $\sim 1900\ M_\odot$.

The prominent KR 81 sub-mm source (JCMTSF J233917.8+615914) has a flux density of 1.2 ± 0.3 Jy within an aperture of 25″ around the peak. The deconvolved radius is $\sim 24''$ and corresponds to a physical diameter of 0.4 pc at a distance of 1.9 ± 0.4 kpc. B_{850} is 0.5 Jy beam^{-1} (S/N of ~ 6.7). This corresponds to a dust-derived peak column density of $N({\rm H_2}) = (2.2 \pm 0.5) \times 10^{22}$ cm^{-2} or $N(M) = 0.10 \pm 0.03$ g cm^{-2}. This dust-based column density is greater than the CO-based column density for the same location, again a possible opacity effect. The mass of the sub-mm source is $27 \pm 13\ M_\odot$. For $T_d = 10$ K, the column density would increase to 6.4×10^{22} cm^{-2} or $N(M) = 0.30$ g cm^{-2} and the mass would increase to 80 $M_\odot$.

The SCUBA Legacy image for KR 81 looks very similar to Figure 10. The main source (JCMTSF J233917.8+615914) is the most prominent one in the catalog with S/N = 13.8, $F_{850} = 2.17$ Jy and $B_{850} = 0.84 \pm 0.06$ Jy beam^{-1}. The corresponding dust-derived peak column density is $N({\rm H_2}) = (3.9 \pm 0.8) \times 10^{22}$ cm^{-2} or $N(M) = 0.18 \pm 0.04$ g cm^{-2} and the corresponding mass is $48 \pm 25\ M_\odot$. This mass is larger than determined in the previous paragraph because of the larger flux, stemming from to the larger source area and peak value in the Legacy catalog. The SCUBA Legacy catalog contains three additional sources near the main source. The sources are listed in Table 3 together with the corresponding peak mass column densities and masses. Five more sources are found near $\ell = 114.^\circ5$, $b = 0.^\circ14$. However the reality of these sources is very questionable as they all have low listed S/N (≤ 3.6) and are located in a region with no detectable CO emission. Therefore we do not include them in our analysis. The SCUBA Legacy catalog has no detected sources around the CO concentration near $\ell = 114.^\circ68$, $b = 0.^\circ12$.

The main KR 81 850 μm source is spatially associated with IRAS 23369+6142 and MSX6C G114.5696+00.2899. The *IRAS* PSC entries are all listed as either good or moderate quality, and the source is detected in all *MSX* bands. Figure 13 shows the SED of this source from 8.3 to 850 μm. Integrating under the curve yields $L_{IR} = 700 \pm 300$ $L_\odot$, where the uncertainty is the combination of the uncertainty in distance and *IRAS* flux density. The measured and calculated quantities are given in Table 2.

Figure 14 shows a composite image of the region ($\sim 2' \times 2'$) surrounding the dominant KR 81 850 μm source, made from 2MASS J-band (Blue), H-band (Green) and $K_{\rm s}$-band (Red) images. The contours are 850 μm brightness levels of 0.15, 0.3, and 0.45 Jy beam^{-1}, and indicate the very central part of the sub-mm source, seen as the darkest small "blob" in Figures 10 and 12. The 2MASS catalog lists five sources within a radius of $\sim 0\overset{\prime}{.}5$ from the location of the peak B_{850}, an area roughly corresponding to the extent of the 850 μm 0.15 Jy beam^{-1} contour. Figure 15 shows these sources plotted in a 2MASS color-color diagram (top) and a color-magnitude diagram for a distance of 1.9 kpc (bottom), like Figure 9. The three sources nearest to the main-sequence/giant branch lines line are probably foreground stars. The two sources with $J - H \geq 2.5$, marked with crosses in Figure 14, could be background giant stars. Star number 1 in Figure 15 is located where a very reddened ($A_V \sim 20$) red giant would be. Star number 2 could be a very reddened Long-Period Variable (LPV) giant star. LPVs are intrinsically very red due to molecular blanketing and cooler continuum temperatures (Bessell & Brett 1988). No obvious embedded YSO candidates are found in the cold dust core detected in the 850 μm image using 2MASS color-color and color-magnitude diagrams.

3.3. KR 120

KR 120 (Sh 2-187) is a 6′ diameter 1420 MHz radio continuum source with a flux density $F_{1420} = 928 \pm 28$ mJy (Kerton 2006). The estimated flux of ionizing photons, $\log N_L = 47.2$ corresponds to a B0 V star (Crowther 2005). Russeil et al. (2007) suggest that a B2.5 V star could be the exciting star for KR 120, but a cluster of such stars would be needed to match the estimated ionizing photon flux. As with KR 7, the identity of the exciting star of this region remains an open question.

For KR 120, the final 850 μm image is shown in Figure 16, and the CO emission associated with the H II region has its peak around −15 km s^{-1} and is mainly concentrated on the Galactic east side (larger Galactic longitude), stretching on the outside of the region demarcated by the *MSX* emission and further up toward the Galactic north above the H II region. There is also a smaller concentration of CO emission to the Galactic southwest (smaller Galactic longitude). Figure 17 shows integrated CO emission from ^{12}CO (left panel, integrated between $-18.0 < V_{\rm LSR} < -8.0$ km s^{-1}) and ^{13}CO (right panel, integrated between $-18.0 < V_{\rm LSR} < -10.0$ km s^{-1}) overlaid with *MSX* A-band contours corresponding to the feature seen in Figure 3. Evidently, even though ^{12}CO and ^{13}CO follow each other fairly well on large scales, the correlation appears to break down for the dense region close to the prominent KR 120 sub-mm source (discussed in the next paragraph), where ^{13}CO and C^{18}O both peak but the ^{12}CO does not (see Figure 18). The $I_{\rm peak}$ of the integrated ^{13}CO emission at the location of the sub-mm source has a value of 39.6 ± 6.0 K km s^{-1}, corresponding to a ^{13}CO-based $N({\rm H}_2) = (2.9 \pm 0.4) \times 10^{22}$ cm^{-2} or $N(M) = 0.13 \pm 0.02$ g cm^{-2}. Similarly, the C^{18}O-based column density is $N({\rm H}_2) = (6.1 \pm 0.9) \times 10^{22}$ cm^{-2} or $N(M) = 0.28 \pm 0.04$ g cm^{-2}, fairly close to the estimate from ^{13}CO. By summing over the entire ^{12}CO feature seen in Figure 17, the mass of the molecular material surrounding KR 120 is estimated to be $\sim 7600\ M_\odot$.

The prominent KR 120 sub-mm source (JCMTSF J012332.0+614849) has a flux density of 1.6 ± 0.4 Jy within an aperture of 18″ around the peak. The deconvolved radius is $\sim 16''$ and corresponds to a physical diameter of 0.2 pc at a distance of 1.44 ± 0.26 kpc. B_{850} is 1.5 Jy beam^{-1} (S/N of ~ 23). This corresponds to a dust-derived peak column density of $N({\rm H}_2) = (7.0 \pm 1.4) \times 10^{22}$ cm^{-2} or $N(M) = 0.33 \pm 0.07$ g cm^{-2}. This dust-based column density is greater than the CO-based column density for the same location, again a possible opacity effect. The mass of the sub-mm source is $21 \pm 9\ M_\odot$. For $T_d = 10$ K, the column density would increase to 2.0×10^{23} cm^{-2} or $N(M) = 0.95$ g cm^{-2} and the mass would increase to 60 $M_\odot$.

The SCUBA Legacy image for KR 120 looks very similar to Figure 16. Apart from the main source, the SCUBA Legacy catalog contains 11 other sources distributed along the fainter 850 μm rims seen in Figure 16. The main source is the most prominent one in the catalog with S/N = 40, $F_{850} = 12.96$ Jy, and $B_{850} = 2.86 \pm 0.07$ Jy beam^{-1}. The corresponding dust-derived peak column density is $N({\rm H}_2) = (1.3 \pm 0.3) \times 10^{23}$ cm^{-2} or $N(M) = 0.62 \pm 0.12$ g cm^{-2}. The corresponding mass is $166 \pm 78\ M_\odot$. This mass derived from the SCUBA Legacy catalog is ~ 8 times greater than the mass found in this work. This is mainly due to the larger area (effective radius of 58″) used in the catalog to obtain the flux, but also the higher peak B_{850}, and it illustrates the systematic uncertainty inherent in the method. We think all the remaining 11 sub-mm sources listed in the Legacy catalog are real detections as they have emission counterparts in our sub-mm maps (although at lower S/N) and are located within, or very close to, the C^{18}O contours shown in Figure 18.

The main KR 120 850 μm source is spatially associated with IRAS 01202+6133 and MSX6C G126.7144-00.8220. In the *IRAS* PSC, 12, 25, and 60 μm flux densities are listed as being good quality flux densities, while the 100 μm flux density only is an upper limit. The source is detected in all *MSX* bands. Figure 19 shows the SED of this source from 8.3 to 850 μm. The arrow indicates an upper limit. Integrating under the curve yields an upper limit of $L_{IR} = 5600\ L_{\odot}$, which is an order of magnitude higher than the other luminosities found in this study. The measured and calculated quantities are given in Table 2.

Figure 20 shows a composite image of the region ($\sim 1.'8 \times 2.'3$) surrounding the dominant KR 120 850 μm source, made from 2MASS J-band (Blue), H-band (Green) and K_{s}-band (Red) images. The contours, 850 μm brightness levels of 0.2, 0.8, and 1.4 Jy beam^{-1}, trace the very central part of the sub-mm source, seen as the darkest small "blob" in Figures 16 and 18. A cluster of 2MASS sources are seen within the 850 μm contours, along with fuzzy NIR emission. The 2MASS catalog lists eight sources, all of which only have upper limit detections in the J-band, within a radius of $\sim 0.'25$ from the location of B_{850}, an area roughly corresponding to the extent of the 850 μm 0.2 Jy beam^{-1} contour. Figure 21 shows these sources plotted in a 2MASS color-color diagram (top) and a color-magnitude diagram for a distance of 1.44 kpc (bottom), like Figure 9. All of the 2MASS sources in the color-color and color-magnitude diagrams have uncertain locations due to high uncertainty in 2MASS magnitudes, but at least almost all of them have to have $H-K \geq 2$, so the sources populate a region where highly embedded intermediate-mass YSOs would be. These 2MASS sources are likely to be a cluster of YSOs.

KR 120 has been the subject of previous studies. Joncas et al. (1992) conducted a multiwavelength study of KR 120 in the optical, IR and radio, and found that KR 120 is an H II region of age $\sim 2 \times 10^5$ years that is still enshrouded in the parental cloud. Zavagno et al. (1994) discovered through spectroscopy a pre-main-sequence object (S 187Hα), located $\sim 2.'2$ from IRAS 01202+6133, and not covered by Figure 20. S 187Hα is spatially located within JCMTSF J012313.2+614959 ($N(M) = 0.18 \pm 0.04$ g cm^{-2} and mass of 25 ± 12 $M_{\odot}$ from Table 3). Salas et al. (1998) imaged the region near IRAS 01202+6133 (S 187 IR) in the NIR and discovered a curved molecular hydrogen outflow nearby that extends over a region of 76$''$ (0.55 pc at 1.44 kpc) that is probably due to a jet from a solar mass YSO; NIRS 1. NIRS 1 is spatially located within JCMTSF J012317.7+614735 ($N(M) = 0.14 \pm 0.03$ g cm^{-2} and mass of 7 ± 3 $M_{\odot}$ from Table 3) and is not covered by Figure 20. Furthermore, the *MSX* source is listed as being associated with an OH maser, a bright signpost for a recently formed massive star (Argon et al. 2000). The presence of the OH maser and pre-main-sequence objects in the neighborhood indicates that the investigated sub-mm clump is likely the site for ongoing star formation, something that agrees with the possible presence of an embedded cluster hinted at in Figures 20 and 21.

4. Discussion

The final list of sub-mm sources associated with the ring-like H II regions includes the three main sources visually identified in our data along with an additional 10 sources for KR 7, 3 for KR 81, and 11 for KR 120 from the SCUBA Legacy catalog (see Table 3 with the three main sources in bold). For consistency we will use the SCUBA Legacy catalog values of derived quantities in this discussion. The masses found for the regions fall within the range of sub-mm masses, $0.5 - 130\ M_{\odot}$, that were found around the previously studied ring-like H II region KR 140 (Kerton et al. 2001). The exception is the main source of KR 120 which is the most massive sub-mm source in the sample with 166 $M_{\odot}$. The visually determined sizes for the three prominent sources, 0.6, 0.4, and 0.2 pc, also fall within the range $0.2 - 0.7$ pc found for sources near KR 140. Around KR 140 as many as 22 sub-mm sources were found, while the three regions in this study have half or that or less. Given the noise level in the sub-mm images and the distances, a 3σ source detection would correspond to a minimum mass sensitivity of $2 - 4\ M_{\odot}$. Only 3 out of 22 sub-mm objects (14%) for KR 140 have a mass $< 2\ M_{\odot}$, so a large population of sub-mm sources is likely not missed in KR 7, KR 81, and KR 120.

Moore et al. (2007) discovered 316 clumps in their 850 μm SCUBA study of the W3 GMC. For this study, we identify a subset of 220 clumps located in the high-density layer (HDL) of the W3 GMC. This layer runs parallel to the W4 H II region and contains a number of luminous, massive star-forming regions (W3 Main, W3 (OH) and AFGL 333) that are likely to be examples of triggered star formation. Using the same dust temperature assumption as above in Section 3 ($T_d = 20$ K) and a distance to W3 of 2.0 kpc, the peak mass column densities and sub-mm clump masses are computed. The distribution of peak mass column densities for the 220 HDL sub-mm sources is displayed in Figure 22 (top). Peak mass column densities range between 0.009 g cm^{-2} and 3.1 g cm^{-2}, with a median of 0.02 g cm^{-2} and an average of 0.07 g cm^{-2}. The distribution of peak mass column densities for KR 7, KR 81 and KR 120 (from Table 3), and for KR 140 (Kerton et al. 2001) is shown in Figure 22 (bottom). The values found for the three prominent KR objects in this study, $0.16 - 0.62$ g cm^{-2}, land above both the median and average value associated with the HDL. Interestingly, while there is overlap in the two mass column density distributions, the HDL distribution is very heavily weighted to lower mass column densities compared to the ring-like H II region distribution. It should be noted though that the maximum peak mass column density for the HDL sources is about an order of magnitude larger than found surrounding the ring-like H II regions.

The masses of the 220 sub-mm sources in the HDL range between 7 and 4900 $M_\odot$, with a median of 31 and an average of 123 $M_\odot$. The sub-mm masses found in this study fall within the range of masses and around the median of masses associated with the HDL, but the maximum masses found within the HDL are at least an order of magnitude higher than found in this study. Figure 23 shows a cumulative plot of sub-mm source mass for the HDL (solid line), KR 7 (triangles), KR 81 (squares), KR 120 (diamonds), and KR 140 (crosses; from Kerton et al. 2001). Table 4 shows the indexes (α) from fitting power laws of the form $N(> M) = N_0 M^{-\alpha}$ to the mass distributions, as well as the fraction of the total mass contained within the first 50% of objects, counting from the smallest to the highest masses. For comparison, a Salpeter (stellar-like) mass distribution would have an index of $\alpha = 1.35$ and the first 50% of objects would have about 18% of the total mass. Except for KR 7, all of the regions we examine have clump mass distributions that are consistent with the typical clump structure index of 0.6 ± 0.1 associated with molecular cloud structure (Kramer et al. 1998; Williams et al. 2000). The KR 7 clumps are an interesting outlier as they have a very steep index (the first 50% of the sources contain about 36% of the total mass) more typical of a stellar initial mass function (IMF) that is usually only seen in smaller (1000 AU scale) structure within molecular clouds (e.g., Motte et al. 1998). However, the KR 7 clumps also span the most limited range of masses of any of the investigated regions.

The respective masses for the surrounding molecular material are 3600 $M_\odot$ within a rough diameter of 19 pc (KR 7), 1900 $M_\odot$ within 12 pc (KR 81), and 7600 $M_\odot$ within 13 pc (KR 120). Ballantyne et al. (2000) found that the molecular cloud surrounding KR 140 contained about 5000 $M_\odot$. Data from the ^{12}CO FCRAO Outer Galaxy Survey (Heyer et al. 1998) with a spectral resolution of 0.98 km s^{-1} and an angular resolution of $46''$ show that the molecular material seen around KR 120 and KR 140 is likely part of larger molecular clouds (subtending $1^\circ - 2^\circ$ on the sky). The material around KR 7 and KR 81 does not show connections to larger molecular clouds. This makes at least two examples of massive stars forming in clouds with masses $< 10^4$ $M_\odot$, which is quite unexpected. Massive stars are expected to form in giant molecular clouds (GMCs), which range $10^4 - 10^6$ $M_\odot$ (Lada & Lada 2003).

Figure 24 shows total integrated luminosity, L_{IR}, as a function of associated clump mass for three types of objects. Ultra-compact H II (UCH II) regions, representing sites of massive star formation are crosses, while intermediate-mass star-forming regions (IM SFRs) are diamonds, both taken from Arvidsson et al. (2010). The three prominent KR sub-mm sources are triangles. Three sources around KR 140 where the identification of infrared sources (IRAS 02174+6052, IRAS 02171+6058 and IRAS 021757+6053) corresponding to sub-mm sources (KMJB 1, KMJB 3 and KMJB 17, 18 and 19) is relatively straightforward is taken from Kerton et al. (2001). It still shows a correlation ($r^2 = 0.89$) between luminosity and associated clump mass for IM SFRs, UCH II regions and KR sub-mm sources. The data are fit by $L \propto M^{1.04\pm0.05}$ which largely agrees with the similar value found for UCH II regions and IM SFRs in Arvidsson et al. (2010), and with the value found for compact H II regions in Chini et al. (1987). From Figure 24 it appears the relationship holds over four orders of magnitude in mass, extending another order of magnitude to lower mass less than found in Arvidsson et al. (2010) and two orders of magnitude lower in mass than shown in Chini et al. (1987). This is significant because a constant ratio of luminosity to associated mass is what is expected if star formation follows the same IMF in all star forming regions and that the star formation efficiency for converting gas into stars is the same over many orders of magnitude in associated mass (Chini et al. 1987).

5. Conclusions

Three ring-like morphology H II regions in the outer Galaxy, KR 7, KR 81, and KR 120 (Sh 2-124, Sh 2-165, and Sh 2-187), have been investigated using SCUBA 850 μm observations and molecular line observations (^{12}CO, ^{13}CO and C^{18}O). They are found to each have one dominant 850 μm source, located in the interface region between the H II region and the surrounding molecular material. At the same location as these dominant 850 μm sources, peaks are found in the integrated molecular spectral maps, confirming these as locations of cold, dense material. Estimating the peak mass column densities toward the dominant sources results in values of $0.1 - 0.6$ g cm^{-2}, comparable to the peak mass column densities found for IM SFRs (Arvidsson et al. 2010). The clump masses associated with the three dominant sources, estimated to be 51, 27, and 21 $M_\odot$, fall within the range of clump masses previously found for KR 140 by Kerton et al. (2001). The same is true for the sizes, 0.6, 0.4, and 0.2 pc, that fall within the range $0.2 - 0.7$ pc. Using 2MASS photometry, a possible embedded cluster of YSOs are found within the dominant sub-mm source of KR 120. This is likely a site for ongoing star formation, consistent with earlier studies that found signatures of star formation in the immediate vicinity. Candidates for embedded YSOs within the sub-mm sources are found for KR 7, while sources toward KR 81 can be explained as either foreground or background objects. Using the SCUBA Legacy catalog, the three H II regions are found to be less populated with sub-mm sources than the previously studied H II region KR 140. All but one of the regions investigated have sub-mm source mass distributions described by shallow sloped (sub-Salpeter) power laws. The exception, KR 7, has a very steep power law fit but covers a much more limited mass range.

The authors thank C. Brunt for providing the CO data. This publication makes use of the NASA/IPAC Infrared Science Archive, which is operated by the Jet Propulsion Laboratory, California Institute of Technology, under contract with the National Aeronautics and Space Administration. This publication makes use of data products from the Two Micron All Sky Survey, which is a joint project of the University of Massachusetts and the Infrared Processing and Analysis Center/California Institute of Technology, funded by the National Aeronautics and Space Administration and the National Science Foundation.

REFERENCES

Argon, A. L., Reid, M. J., & Menten, K. M. 2000, ApJS, 129, 159

Arvidsson, K., Kerton, C. R., Alexander, M. J., Kobulnicky, H. A., & Uzpen, B. 2010, AJ, 140, 462

Ballantyne, D. R., Kerton, C. R., & Martin, P. G. 2000, ApJ, 539, 283

Bessell, M. S., & Brett, J. M. 1988, PASP, 100, 1134

Chini, R., Kruegel, E., & Wargau, W. 1987, A&A, 181, 378

Crampton, D., & Fisher, W. A. 1974, Publ. Dom. Astrophys. Obs. Victoria, 14, 283

Crampton, D., Georgelin, Y. M., & Georgelin, Y. P. 1978, A&A, 66, 1

Crowther, P. A. 2005, in IAU Symp. 227, Massive Star Birth: A Crossroads of Astrophysics, ed. R. Cesaroni, M. Felli, E. Churchwell, &

M. Walmsley (Cambridge: Cambridge Univ. Press), 389

Deharveng, L., Zavagno, A., & Caplan, J. 2005, A&A, 433, 565

Di Francesco, J., Johnstone, D., Kirk, H., MacKenzie, T., & Ledwosinska, E. 2008, ApJS, 175, 277

Elmegreen, B. G. 1998, in ASP Conf. Ser. 148, Origins, ed. C. E. Woodward, J. M. Shull, & H. A. Thronson, Jr. (San Francisco, CA: ASP), 150

Emerson, J. P. 1988, in NATO ASIC Proc. 241, Formation and Evolution of Low Mass Stars, ed. A. K. Dupree & M. T. V. T. Lago (Dordrecht: Kluwer), 193

Foster, T., & Routledge, D. 2003, ApJ, 598, 1005

Heyer, M. H., Brunt, C., Snell, R. L., Howe, J. E., Schloerb, F. P., & Carpenter, J. M. 1998, ApJS, 115, 241

Hunter, D. A., & Massey, P. 1990, AJ, 99, 846

Jackson, J. M., et al. 2006, ApJS, 163, 145

Johnstone, D., Wilson, C. D., Moriarty-Schieven, G., Giannakopoulou-Creighton, J., & Gregersen, E. 2000, ApJS, 131, 505

Joncas, G., Durand, D., & Roger, R. S. 1992, ApJ, 387, 591

Kallas, E. & Reich, W. 1980, A&AS, 42, 227

Kauffmann, J., Bertoldi, F., Bourke, T. L., Evans, N. J., II, & Lee, C. W. 2008, A&A, 487, 993

Kerton, C. R. 2006, MNRAS, 373, 1203

Kerton, C. R., Arvidsson, K., Knee, L. B. G., & Brunt, C. 2008, MNRAS, 385, 995

Kerton, C. R., Ballantyne, D. R., & Martin, P. G. 1999, AJ, 117, 2485

Kerton, C. R., Martin, P. G., Johnstone, D., & Ballantyne, D. R. 2001, ApJ, 552, 601

Koornneef, J. 1983, A&A, 128, 84

Kramer, C., Stutzki, J., Rohrig, R., & Corneliussen, U. 1998, A&A, 329, 249

Lada, C. J., & Lada, E. A. 2003, ARA&A, 41, 57

Lahulla, J. F. 1985, A&AS, 61, 537

Moore, T. J. T., Bretherton, D. E., Fujiyoshi, T., Ridge, N. A., Allsopp, J., Hoare, M. G., Lumsden, S. L., & Richer, J. S. 2007, MNRAS, 379, 663

Motte, F., Andre, P., & Neri, R. 1998, A&A, 336, 150

Price, S. D., Egan, M. P., Carey, S. J., Mizuno, D. R., & Kuchar, T. A. 2001, AJ, 121, 2819

Rieke, G. H., & Lebofsky, M. J. 1985, ApJ, 288, 618

Rohlfs, K., & Wilson, T. L. 2004, Tools of Radio Astronomy (4th ed.; New York: Springer)

Rudolph, A. L., Brand, J., de Geus, E. J., & Wouterloot, J. G. A. 1996, ApJ, 458, 653

Russeil, D., Adami, C., & Georgelin, Y. M. 2007, A&A, 470, 161

Salas, L., Cruz-Gonzalez, I., & Porras, A. 1998, ApJ, 500, 853

Sharpless, S. 1959, ApJS, 4, 257

Simon, R., Jackson, J. M., Clemens, D. P., Bania, T. M., & Heyer, M. H. 2001, ApJ, 551, 747

Taylor, A. R., et a. 2003, AJ, 125, 3145

Williams, J. P., Blitz, L., & McKee, C. F. 2000, in Protostars and Planets IV, ed. V. Mannings, A. P. Boss, & S. S. Russell (Tucson, AZ: Univ. Arizona Press), 97

Zavagno, A., Deharveng, L., & Caplan, J. 1994, A&A, 281, 491

This 2-column preprint was prepared with the AAS LATEX macros v5.2.

Table 1

Table of the Investigated Regions.

Region	R.A. (h m s)	Decl. (° ′ ″)	ℓ (°)	b (°)	Distance (kpc)	Designations
KR 7	21 38 17.0	+50 19 48	94.461	-1.549	2.8 ± 0.4^{a}	Sh 2-124, LBN 426
KR 81	23 39 43.7	+61 54 58	114.600	0.210	1.9 ± 0.4^{a}	Sh 2-165, LBN 565
KR 120	01 22 58.0	+61 48 16	126.647	-0.840	1.44 ± 0.26^{b}	Sh 2-187, LBN 630

Note.—Coordinates are J2000.

[a] From Foster & Routledge (2003).

[b] From Russeil et al. (2007).

Table 2

Results of Analysis of the Three Main 850 μm Sources.

Region	KR 7	KR 81	KR 120
JCMTSF	J213822.5+501908	J233917.8+615914	J012332.0+614849
$I^{a}_{\rm peak}$ (K km s^{-1})	7.9 ± 1.2	13.5 ± 2.0	39.6 ± 6.0
$I^{b}_{\rm peak}$ (K km s^{-1})	···	1.3 ± 0.2	8.1 ± 1.2
Radius (″)	24	24	16
F_{850} (Jy)	1.1 ± 0.2	1.2 ± 0.3	1.6 ± 0.4
B_{850} (Jy beam^{-1})	0.50 ± 0.11	0.48 ± 0.12	1.52 ± 0.31
$N(M)^{a}_{\rm peak}$ (g cm^{-2})	0.026 ± 0.004	0.045 ± 0.007	0.13 ± 0.02
$N(M)^{b}_{\rm peak}$ (g cm^{-2})	···	0.045 ± 0.007	0.28 ± 0.04
$N(M)^{c}_{\rm peak}$ (g cm^{-2})	0.11 ± 0.02	0.10 ± 0.03	0.33 ± 0.07
Diameter (pc)	0.6	0.4	0.2
Mass^{c} ($M_{\odot}$)	51 ± 19	27 ± 13	21 ± 9
$N(M)^{d}_{\rm peak}$ (g cm^{-2})	0.16 ± 0.03	0.18 ± 0.04	0.62 ± 0.12
Mass^{d} ($M_{\odot}$)	78 ± 32	48 ± 25	166 ± 78
MSX6C	G094.4674-01.5705	G114.5696+00.2899	G126.7144-00.8220
$F_{\rm A}$ (Jy)	$0.554 \pm 4.4\%$	$2.60 \pm 4.1\%$	$8.21 \pm 4.1\%$
$F_{\rm C}$ (Jy)	···	$3.83 \pm 5.2\%$	$12.6 \pm 5.0\%$
$F_{\rm E}$ (Jy)	···	$5.47 \pm 6.2\%$	$105 \pm 6.0\%$
IRAS	21366+5005	23369+6142	01202+6133
F_{12} (Jy)	$0.94 \pm 5\%$	$5.025 \pm 8\%$	$10.44 \pm 8\%$
F_{25} (Jy)	$1.60 \pm 7\%$	$8.322 \pm 6\%$	$182.3 \pm 4\%$
F_{60} (Jy)	$14.0 \pm 18\%$	$37.5 \pm 12\%$	$881.5 \pm 6\%$
F_{100} (Jy)	≤ 66.3	$153.8 \pm 18\%$	≤ 1716
$L_{\rm IR}$ ($L_{\odot}$)	≤ 500	700 ± 300	≤ 5600

Note.—[a] Based on ^{13}CO.

[b] Based on C^{18}O.

[c] Based on 850 μm.

[d] From Table 3.

Table 3
SCUBA Legacy 850 μm Sources.

Region	Source JCMTSF	ℓ (°)	b (°)	B_{850} (Jy beam^{-1})	S/N	F_{850} (Jy)	$N(M)_{\rm peak}$ (g cm^{-2})	Mass ($M_\odot$)
KR 7	**J213822.5+501908**	**94.4642**	**−1.5675**	**0.73**	**13.0**	**1.62**	**0.16 ± 0.03**	**78 ± 32**
KR 7	J213825.8+502714	94.5605	−1.4724	0.25	4.4	1.35	0.05 ± 0.02	65 ± 27
KR 7	J213801.8+501956	94.4319	−1.5209	0.23	4.2	0.58	0.05 ± 0.01	28 ± 12
KR 7	J213756.2+502344	94.4630	−1.4637	0.23	4.1	0.84	0.05 ± 0.02	41 ± 17
KR 7	J213749.9+502102	94.4205	−1.4862	0.23	4.1	0.83	0.05 ± 0.02	40 ± 17
KR 7	J213813.7+501908	94.4467	−1.5519	0.21	3.9	1.06	0.05 ± 0.01	51 ± 21
KR 7	J213753.1+502308	94.4502	−1.4657	0.21	3.7	0.75	0.05 ± 0.02	36 ± 15
KR 7	J213835.7+502137	94.5180	−1.5599	0.19	3.3	0.41	0.04 ± 0.02	20 ± 8
KR 7	J213803.0+501850	94.4221	−1.5367	0.19	3.5	0.71	0.04 ± 0.01	34 ± 14
KR 7	J213759.9+501908	94.4193	−1.5275	0.19	3.5	0.68	0.04 ± 0.01	33 ± 14
KR 7	J213749.3+502202	94.4304	−1.4727	0.19	3.3	1.12	0.04 ± 0.02	54 ± 22
KR 81	**J233917.8+615914**	**114.5707**	**0.2923**	**0.84**	**13.8**	**2.17**	**0.18 ± 0.04**	**48 ± 25**
KR 81	J233922.3+615702	114.5691	0.2546	0.46	7.6	2.47	0.10 ± 0.02	55 ± 28
KR 81	J233923.7+615938	114.5837	0.2955	0.36	5.9	0.67	0.08 ± 0.02	15 ± 8
KR 81	J233912.1+615649	114.5489	0.2566	0.25	4.1	1.29	0.05 ± 0.02	29 ± 15
KR 120	**J012332.0+614849**	**126.7127**	**−0.8223**	**2.86**	**40.0**	**12.96**	**0.62 ± 0.12**	**166 ± 78**
KR 120	J012338.8+614819	126.7270	−0.8289	1.16	16.2	5.83	0.25 ± 0.05	75 ± 35
KR 120	J012329.0+615336	126.6969	−0.7439	0.86	12.1	3.71	0.19 ± 0.04	47 ± 22
KR 120	J012313.2+614959	126.6736	−0.8076	0.82	11.5	1.93	0.18 ± 0.04	25 ± 12
KR 120	J012317.7+614735	126.6873	−0.8462	0.67	9.7	0.58	0.14 ± 0.03	7 ± 3
KR 120	J012328.9+615424	126.6951	−0.7307	0.61	8.3	1.75	0.13 ± 0.03	22 ± 11
KR 120	J012318.8+615312	126.6779	−0.7530	0.48	6.8	1.49	0.10 ± 0.03	19 ± 9
KR 120	J012338.5+615201	126.7187	−0.7678	0.44	6.2	1.45	0.09 ± 0.02	19 ± 9
KR 120	J012342.8+615114	126.7287	−0.7797	0.42	5.9	2.04	0.09 ± 0.02	26 ± 12
KR 120	J012250.4+614951	126.6293	−0.8153	0.38	5.5	1.61	0.08 ± 0.02	21 ± 10
KR 120	J012321.2+615454	126.6791	−0.7243	0.38	4.9	1.00	0.08 ± 0.02	13 ± 6
KR 120	J012313.6+614653	126.6807	−0.8588	0.36	5.0	0.34	0.08 ± 0.02	4 ± 2

Note.—Final sample of sub-mm sources considered for comparisons. The three main sources are shown in bold. Columns 2 − 7 are taken from Di Francesco et al. (2008). Column 8 is calculated using an absolute flux uncertainty of 20%. Column 9 is calculated using a flux density uncertainty of 30%.

Table 4
Mass Distribution Characteristics.

Region	α	50% Mass Values	N
KR 7	1.8 ± 0.2	36%	11
KR 81	0.9 ± 0.3	30%	4
KR 120	0.72 ± 0.08	19%	12
KR 140	0.50 ± 0.04	7%	22
W3 HDL	0.76 ± 0.01	6%	220

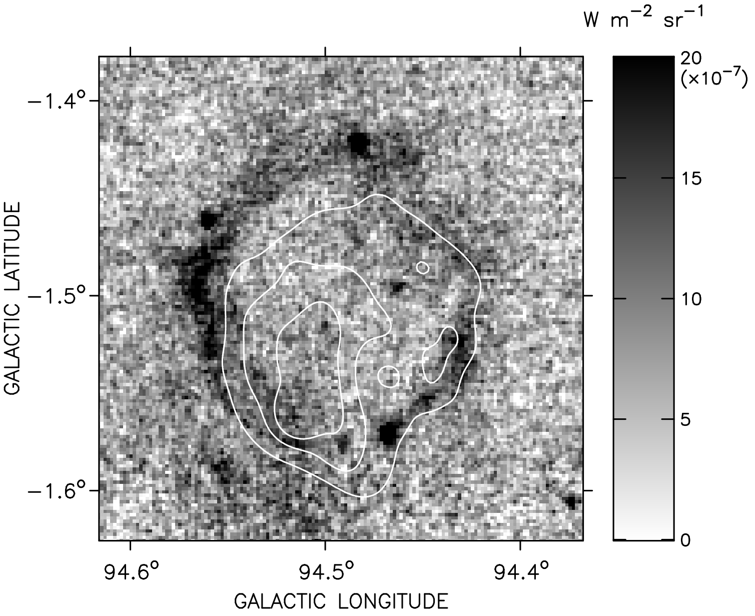

Fig. 1.— *MSX* 8.3 μm image of KR 7 (Sh 2-124). The white contours correspond to CGPS 1420 MHz continuum brightness temperature levels of 11, 13, and 15 K.

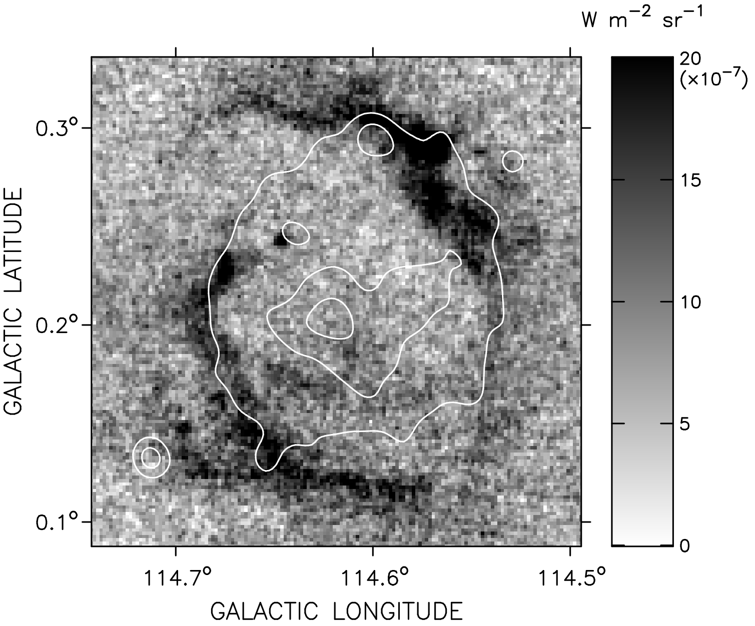

Fig. 2.— *MSX* 8.3 μm image of KR 81 (Sh 2-165). The white contours correspond to CGPS 1420 MHz continuum brightness temperature levels of 7, 8, and 9 K.

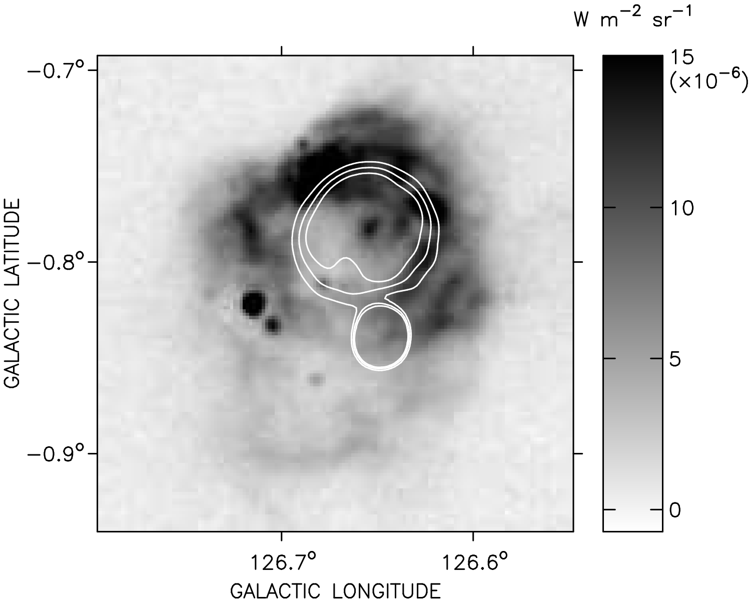

Fig. 3.— *MSX* 8.3 μm image of KR 120 (Sh 2-187). The white contours correspond to CGPS 1420 MHz continuum brightness temperature levels of 10, 12, and 14 K. The radio source seen at the edge of the main H II region contours is an extragalactic background source.

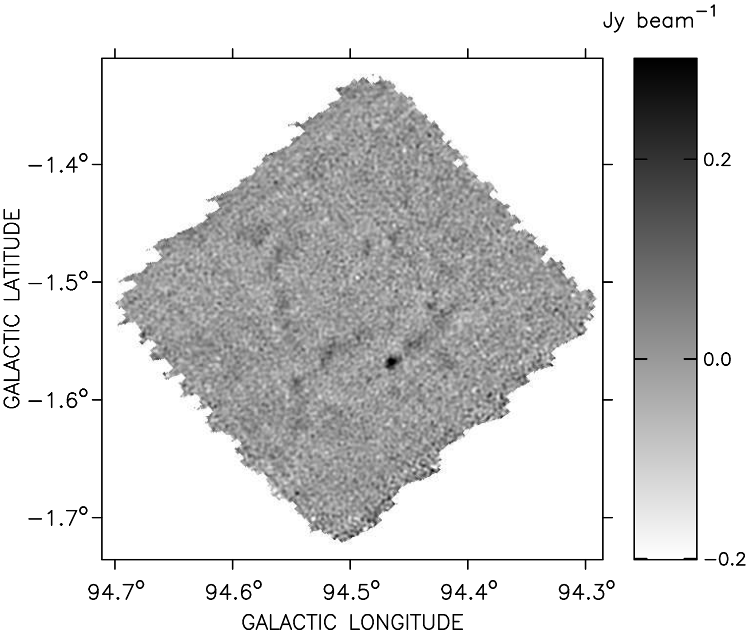

Fig. 4.— Final 850 μm image of KR 7.

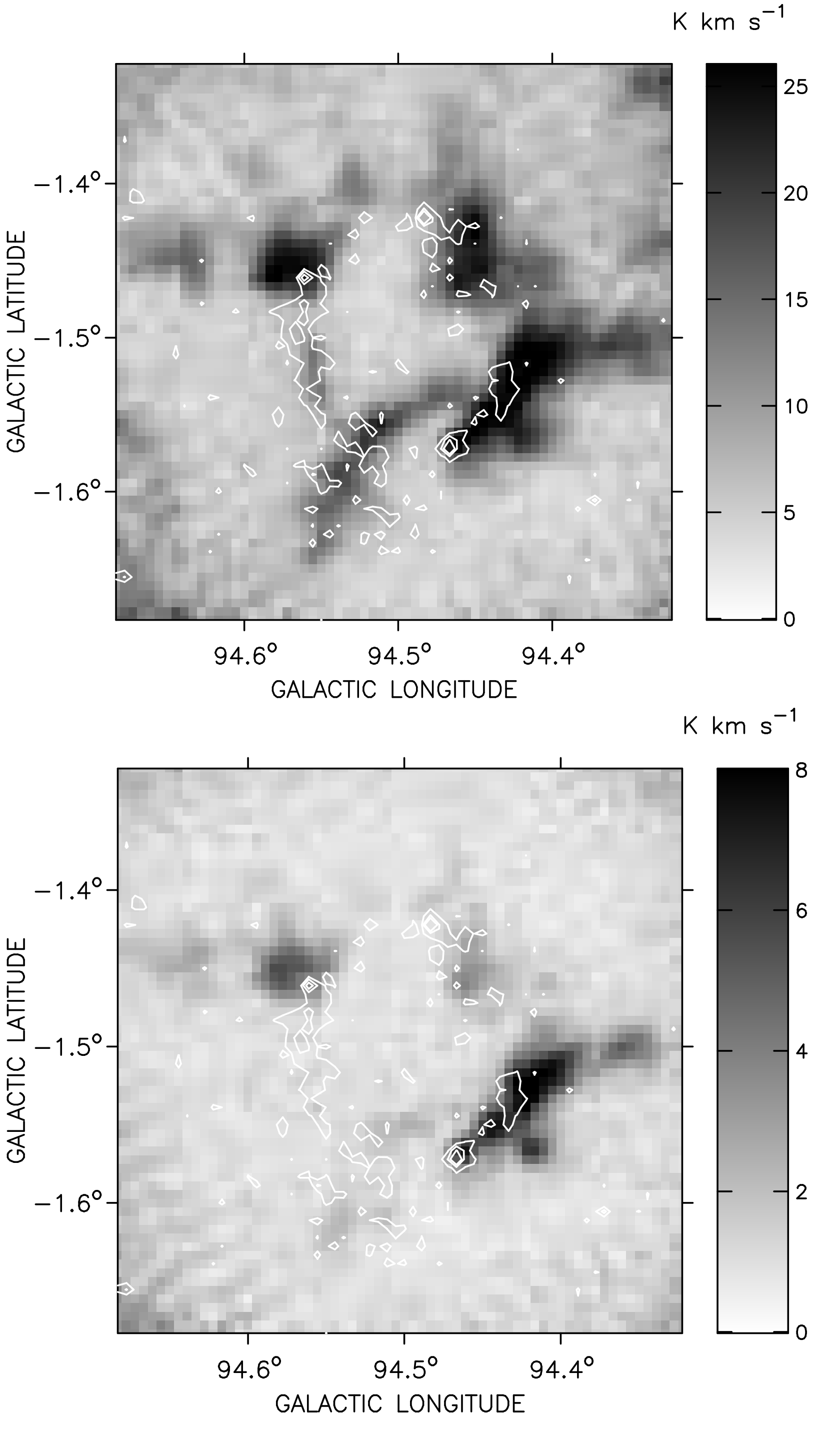

Fig. 5.— Top: integrated ^{12}CO emission around KR 7. Bottom: integrated ^{13}CO emission around KR 7. The white contours correspond to *MSX* brightness levels of 1.3×10^{-6}, 2×10^{-6}, and 3×10^{-6} W m^{-2} sr^{-1} from Figure 1.

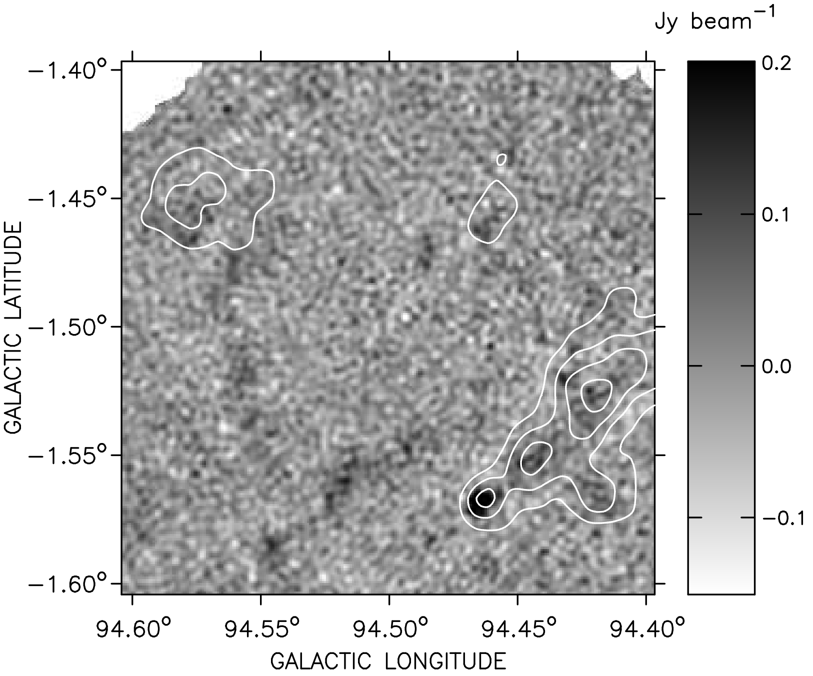

Fig. 6.— Close up view of KR 7 in 850 μm. The white contours correspond to integrated ^{13}CO brightness levels of 3, 5, 7, and 9 K km s^{-1}.

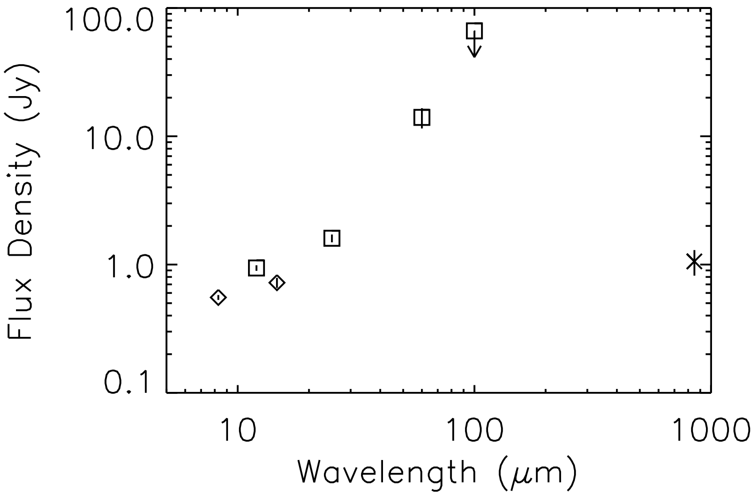

Fig. 7.— Spectral energy distribution for the KR 7 850 μm source. *IRAS* PSC values are squares, *MSX6C* PSC values are diamonds and the 850 μm value is the cross. The vertical lines drawn on each symbol indicate $\pm 1\sigma$ uncertainty for each value. The arrow indicates an upper limit.

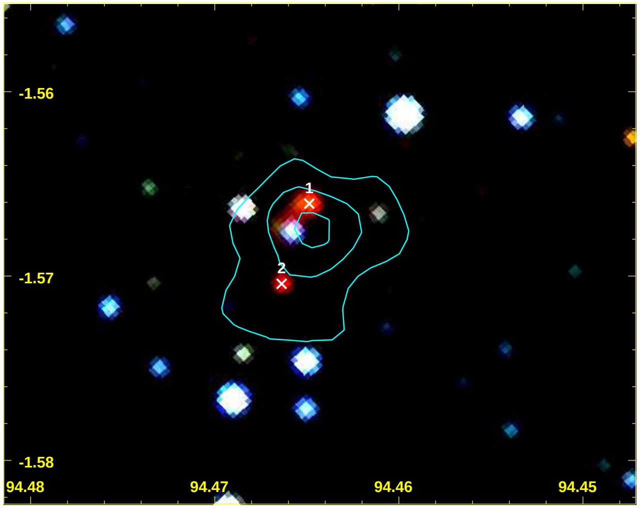

Fig. 8.— $\sim 1\farcm6 \times 2'$ RGB composite of 2MASS J-band (Blue), H-band (Green) and K_s-band (Red) images of KR 7. The contours correspond to 850 μm brightness levels of 0.15, 0.3, and 0.45 Jy beam^{-1}. The crosses are the two possible embedded YSOs, labeled "1" and "2" in Figure 9.

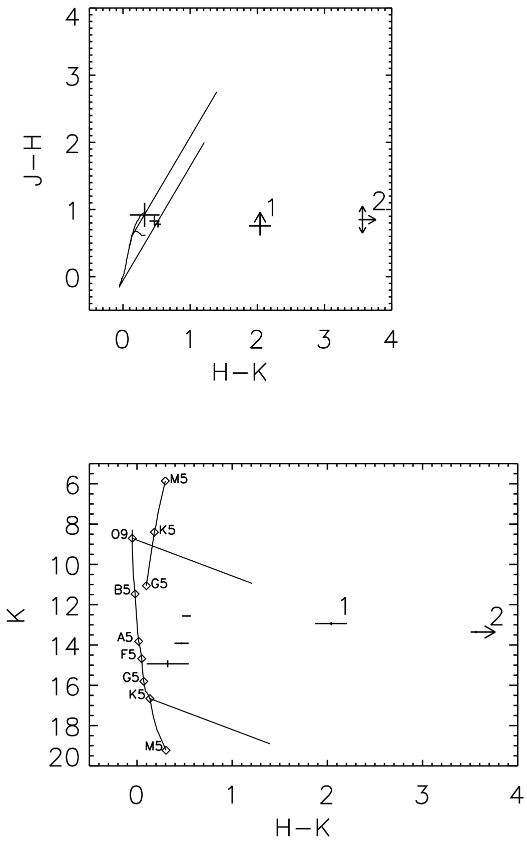

Fig. 9.— Top: color-color diagram for the 2MASS sources within a radius of $0\farcm25$ of the KR 7 850 μm source. The solid lines in the lower left corner show the intrinsic colors of main-sequence (V) and giant (III) stars. The parallel lines show $A_V = 20$ reddening vectors for a K5 V and a O9 V star. Bottom: color-magnitude diagram for the same 2MASS sources at a distance of 2.8 kpc. The main-sequence and giant branch are shown with some representative spectral types. The parallel lines are again $A_V = 20$ reddening vectors. The size of the plotted crosses for the 2MASS sources indicates the uncertainty in 2MASS photometry. An arrow indicates sources where the 2MASS catalog only lists an upper brightness limit in the relevant band. The three sources near the main-sequence lines are probably foreground stars. The two sources labeled "1" and "2" are the two possible embedded YSOs.

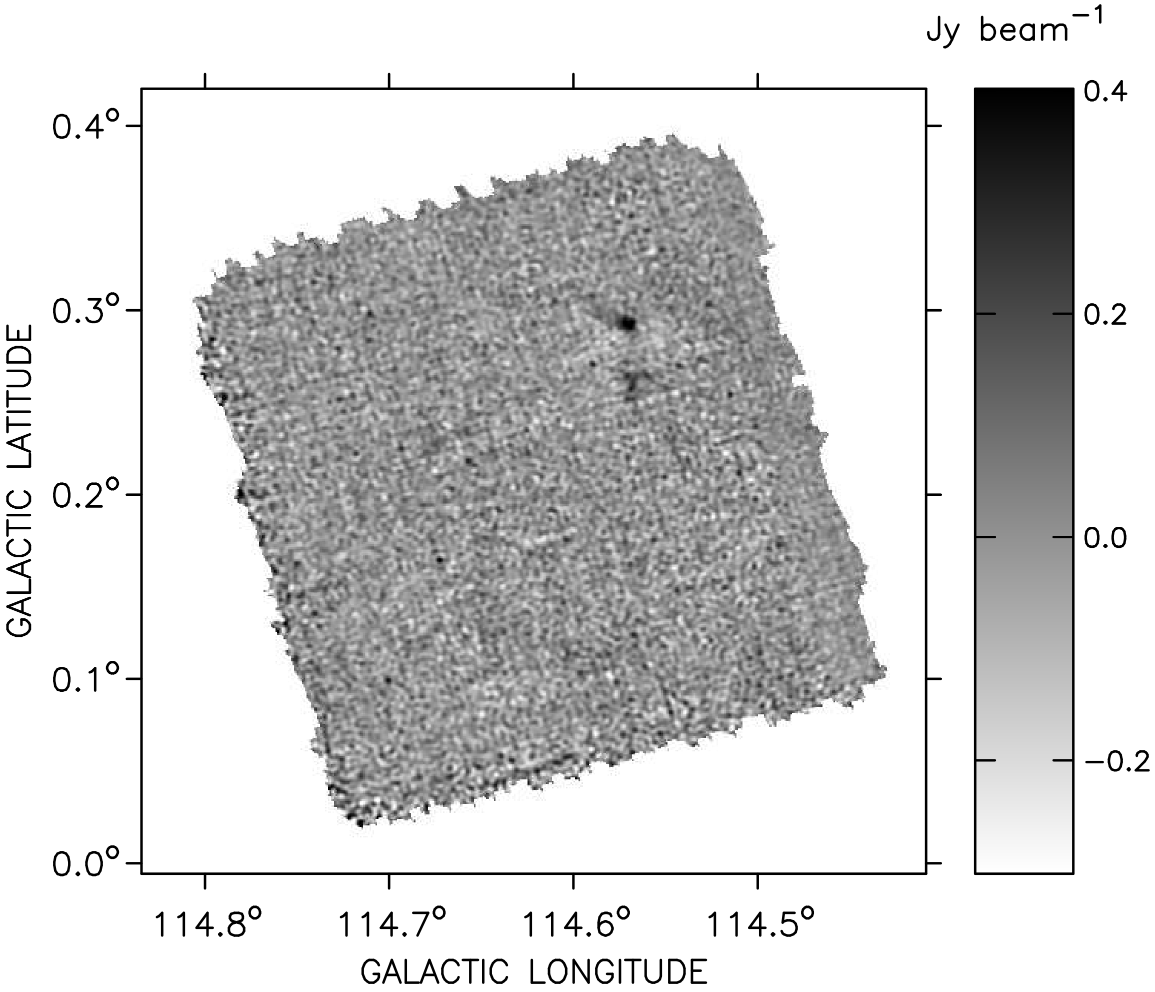

Fig. 10.— Final 850 μm image of KR 81.

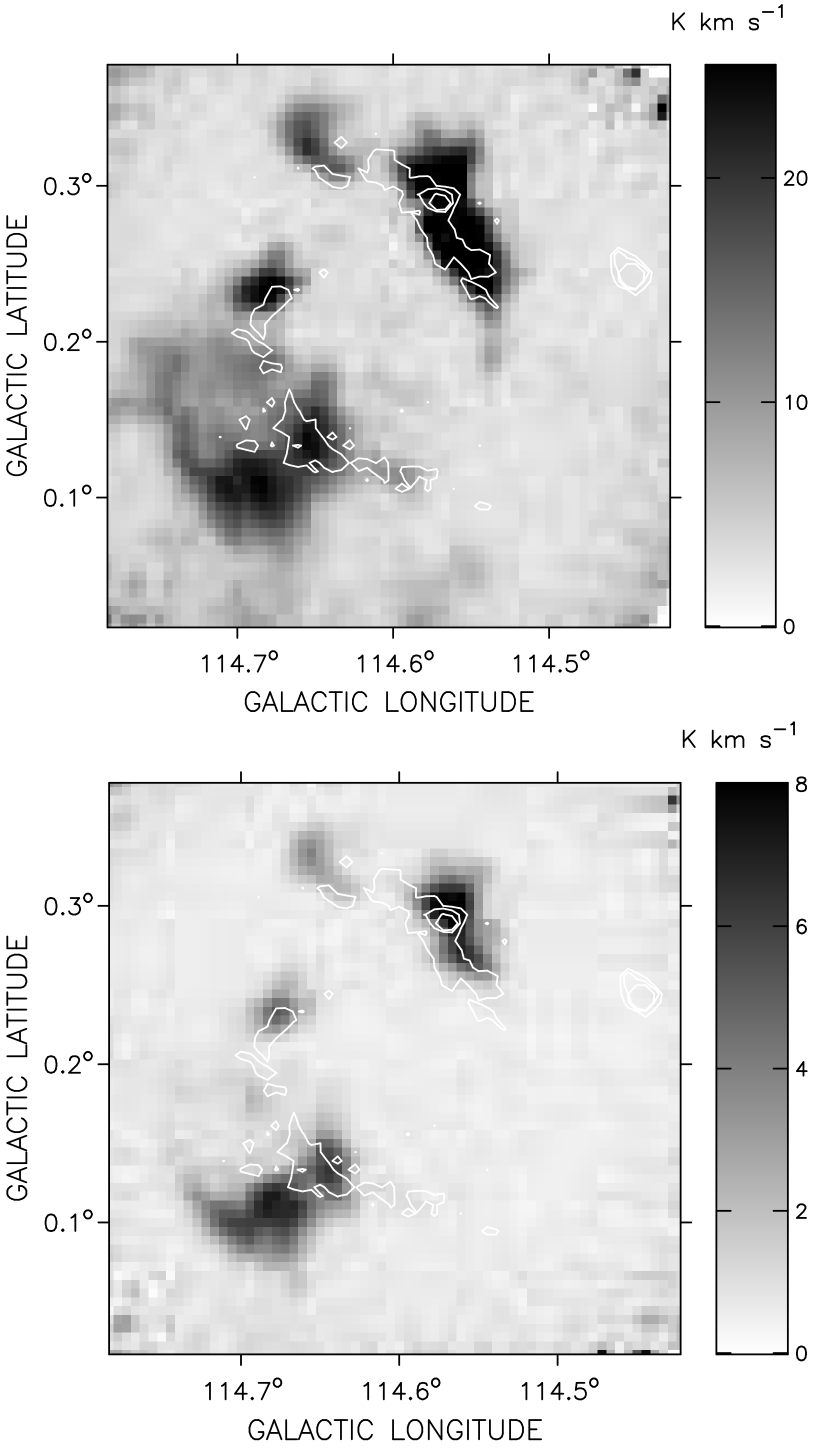

Fig. 11.— Top: integrated ^{12}CO emission around KR 81. Bottom: integrated ^{13}CO emission around KR 81. The white contours correspond to *MSX* brightness levels of 1.5×10^{-6}, 3×10^{-6}, and 6×10^{-6} W m^{-2} sr^{-1} from Figure 2.

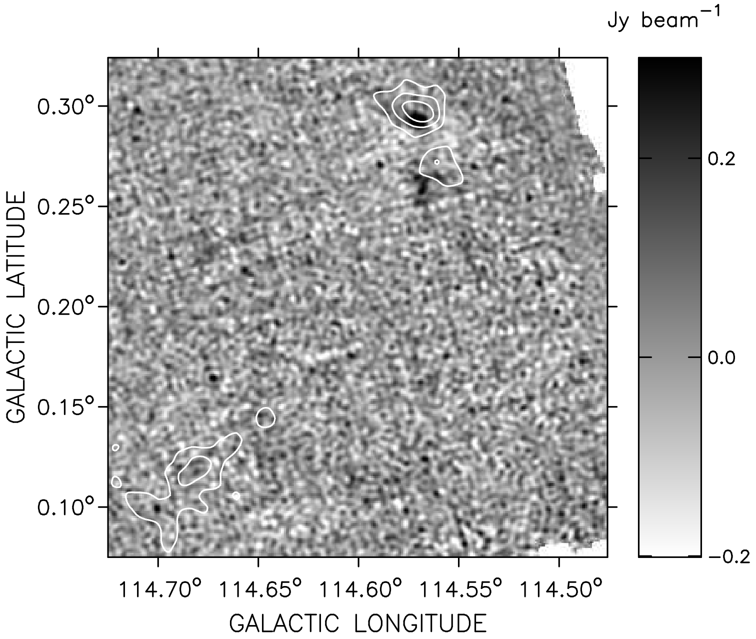

Fig. 12.— Close up view of KR 81 in 850 μm. The white contours correspond to integrated $C^{18}O$ brightness levels of 0.5, 0.75, and 1.0 K km s^{-1}.

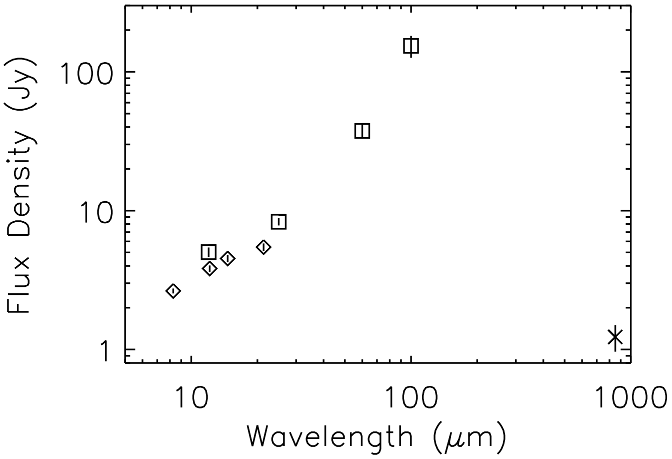

Fig. 13.— Spectral energy distribution for the KR 81 850 μm source. *IRAS* PSC values are squares, *MSX6C* PSC values are diamonds and the 850 μm value is the cross. The vertical lines drawn on each symbol indicate ±1σ uncertainty for each value.

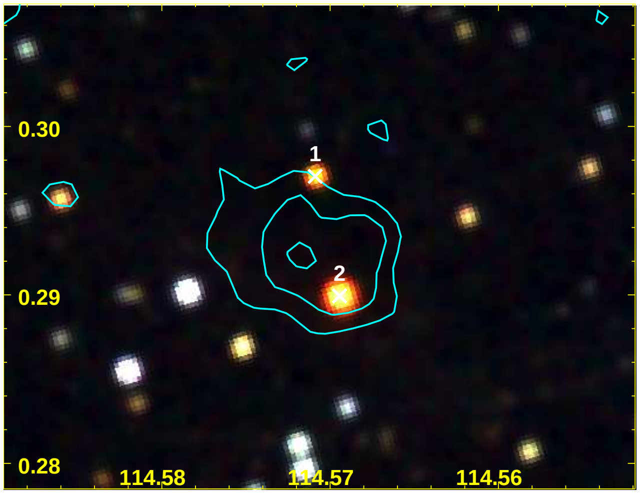

Fig. 14.— $\sim 2' \times 2'$ RGB composite of 2MASS J-band (Blue), H-band (Green) and K_s-band (Red) images of KR 81. The contours correspond to 850 μm brightness levels of 0.15, 0.3, and 0.45 Jy beam^{-1}. The crosses are the two possible background giant stars, labeled "1" and "2" in Figure 15.

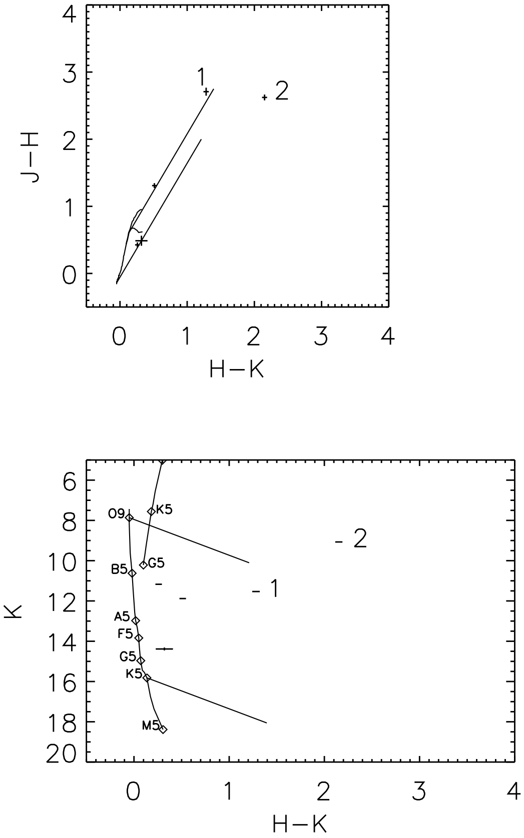

Fig. 15.— Top: color-color diagram for the 2MASS sources within a radius of 0$'\!.$5 of the KR 81 850 μm source. The solid lines in the lower left corner show the intrinsic colors of main-sequence (V) and giant (III) stars. The parallel lines show $A_V = 20$ reddening vectors for a K5 V and a O9 V star. Bottom: color-magnitude diagram for the same 2MASS sources at a distance of 1.9 kpc. The main-sequence and giant branch are shown with some representative spectral types. The parallel lines are again $A_V = 20$ reddening vectors. The size of the plotted crosses for the 2MASS sources indicates the uncertainty in 2MASS photometry. The three sources near the main-sequence lines are probably foreground stars. The two sources labeled "1" and "2" are the two possible background giant stars.

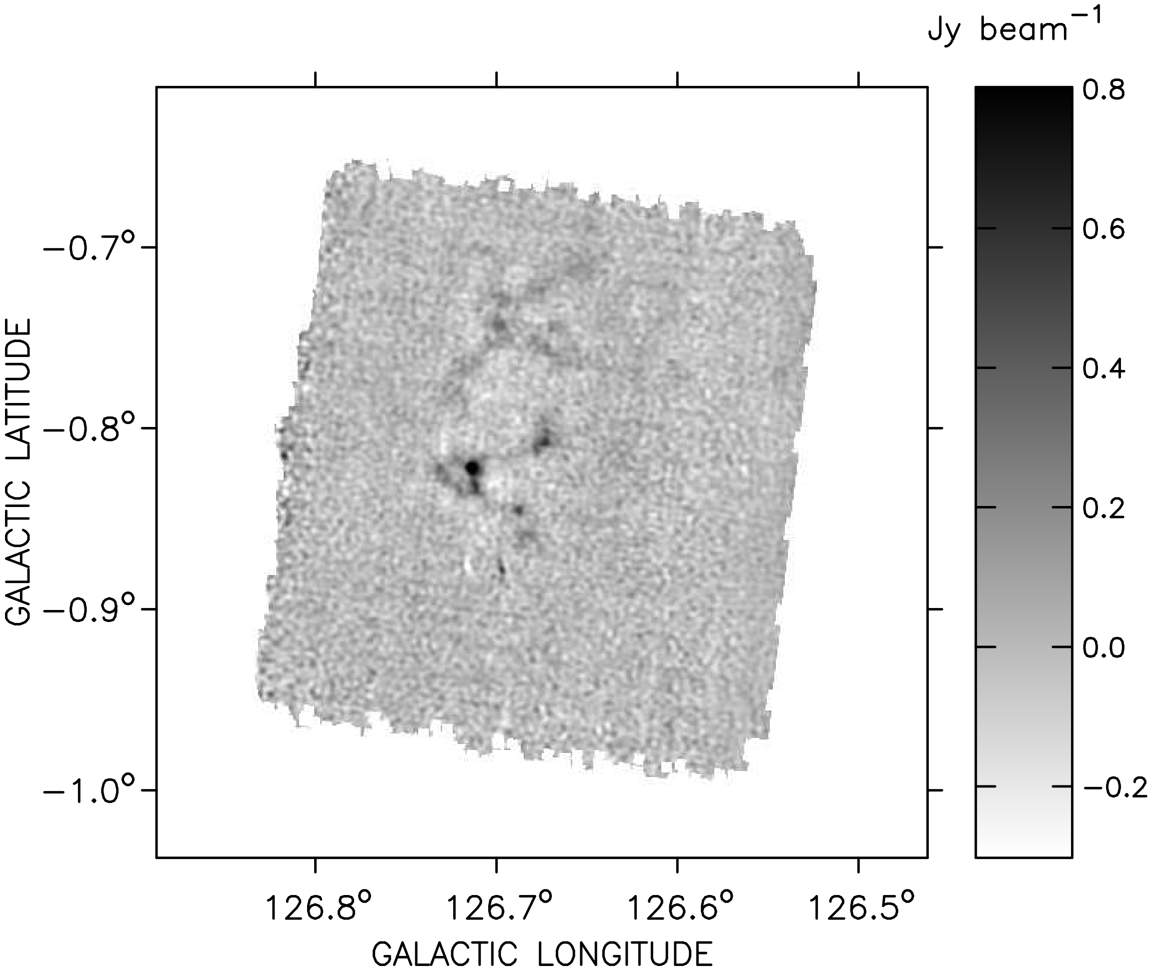

Fig. 16.— Final 850 μm image of KR 120.

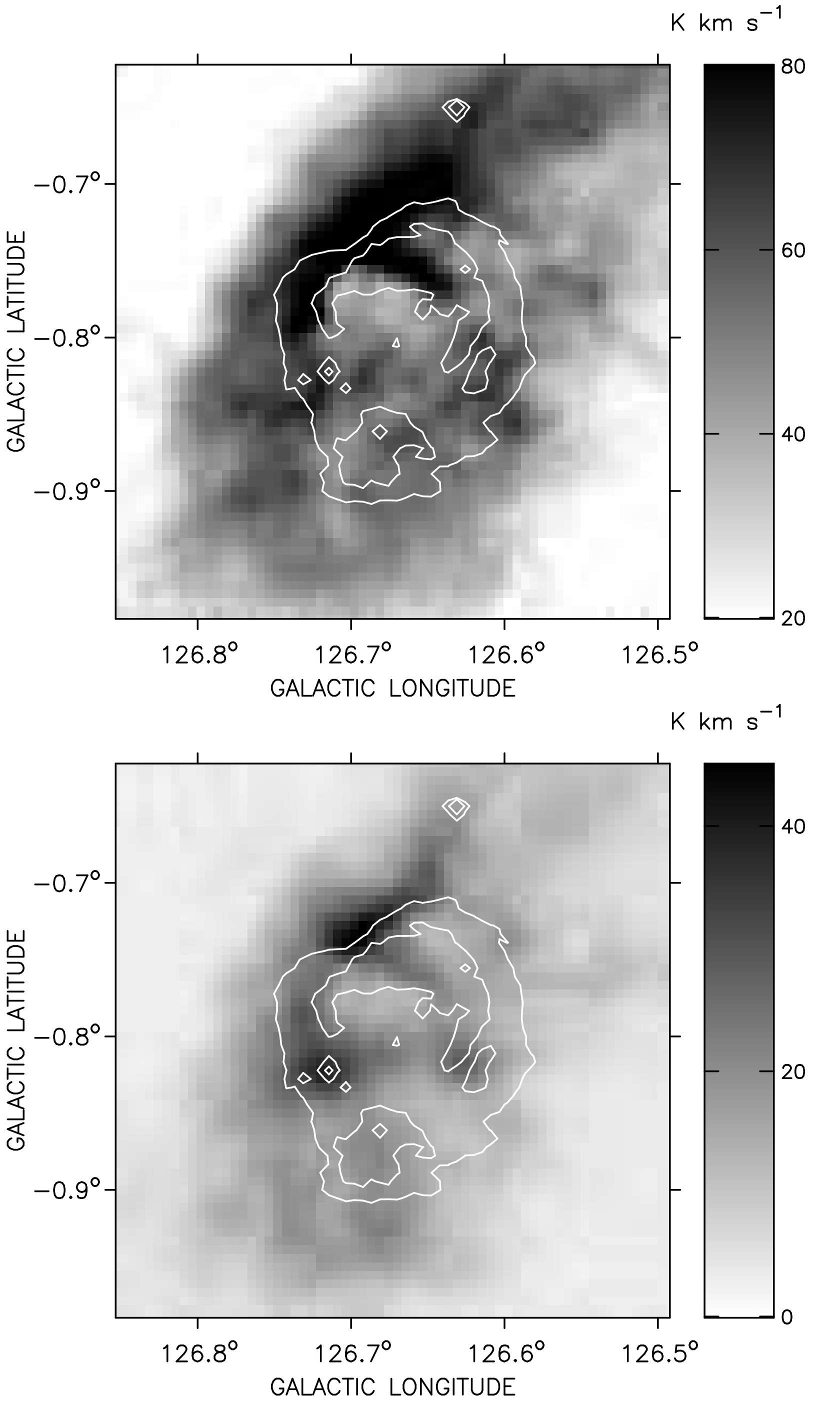

Fig. 17.— Top: integrated ^{12}CO emission around KR 120. Bottom: integrated ^{13}CO emission around KR 120. The white contours correspond to *MSX* brightness levels of 3×10^{-6}, 1×10^{-5}, and 5×10^{-5} W m^{-2} sr^{-1} from Figure 3.

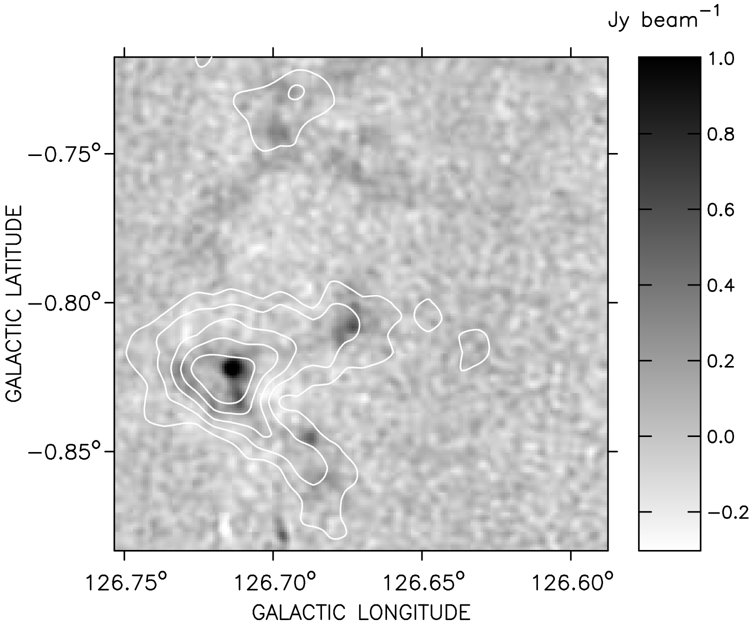

Fig. 18.— Close up view of KR 120 in 850 μm. The white contours correspond to integrated $C^{18}O$ brightness levels of 3, 4, 5, 6, and 7 K km s^{-1}.

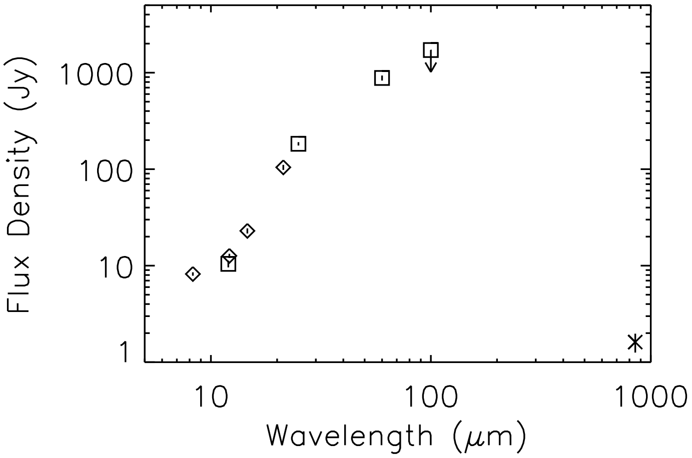

Fig. 19.— Spectral energy distribution for the KR 120 850 μm source. *IRAS* PSC values are squares, *MSX6C* PSC values are diamonds and the 850 μm value is the cross. The vertical lines drawn on each symbol indicate $\pm1\sigma$ uncertainty for each value. The arrow indicates an upper limit.

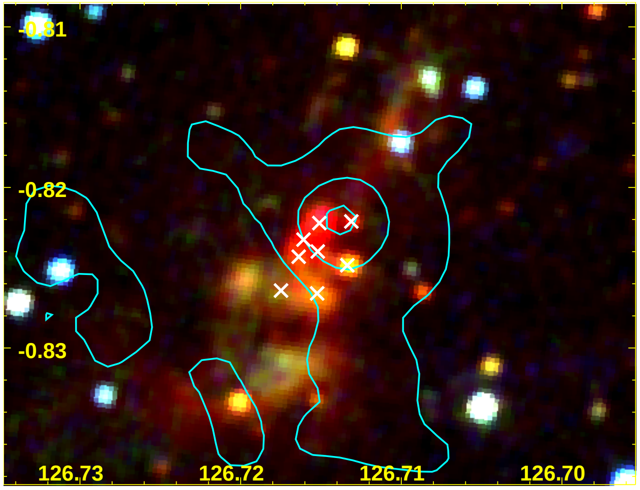

Fig. 20.— ~ 1.′8 × 2.′3 RGB composite of 2MASS *J*-band (Blue), *H*-band (Green) and K_s-band (Red) images of KR 120. The contours correspond to 850 μm brightness levels of 0.2, 0.8, and 1.4 Jy beam^{-1}.

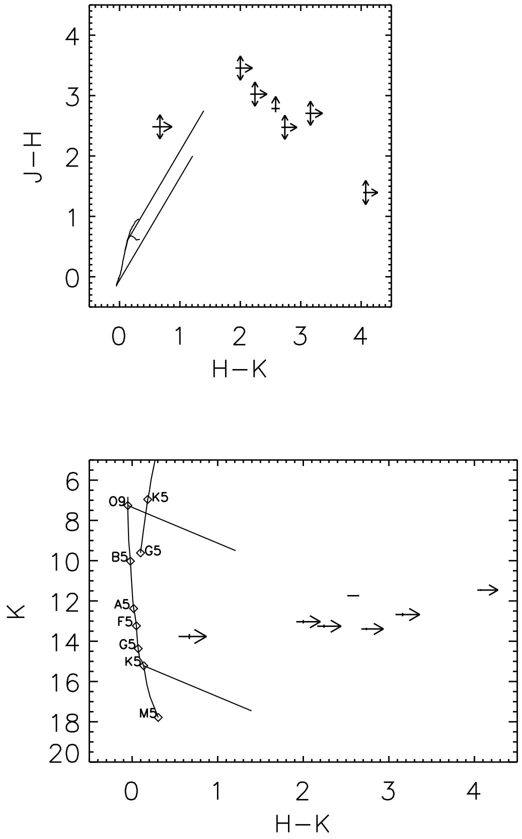

Fig. 21.— Top: color-color diagram for the 2MASS sources within a radius of 0.′25 of the KR 120 850 μm source. The solid lines in the lower left corner show the intrinsic colors of main-sequence (V) and giant (III) stars. The parallel lines show $A_V = 20$ reddening vectors for a K5 V and a O9 V star. Bottom: color-magnitude diagram for the same 2MASS sources at a distance of 1.44 kpc. The main-sequence and giant branch are shown with some representative spectral types. The parallel lines are again $A_V = 20$ reddening vectors. The size of the plotted crosses for the 2MASS sources indicates the uncertainty in 2MASS photometry. An arrow indicates sources where the 2MASS catalog only lists an upper brightness limit in the relevant band.

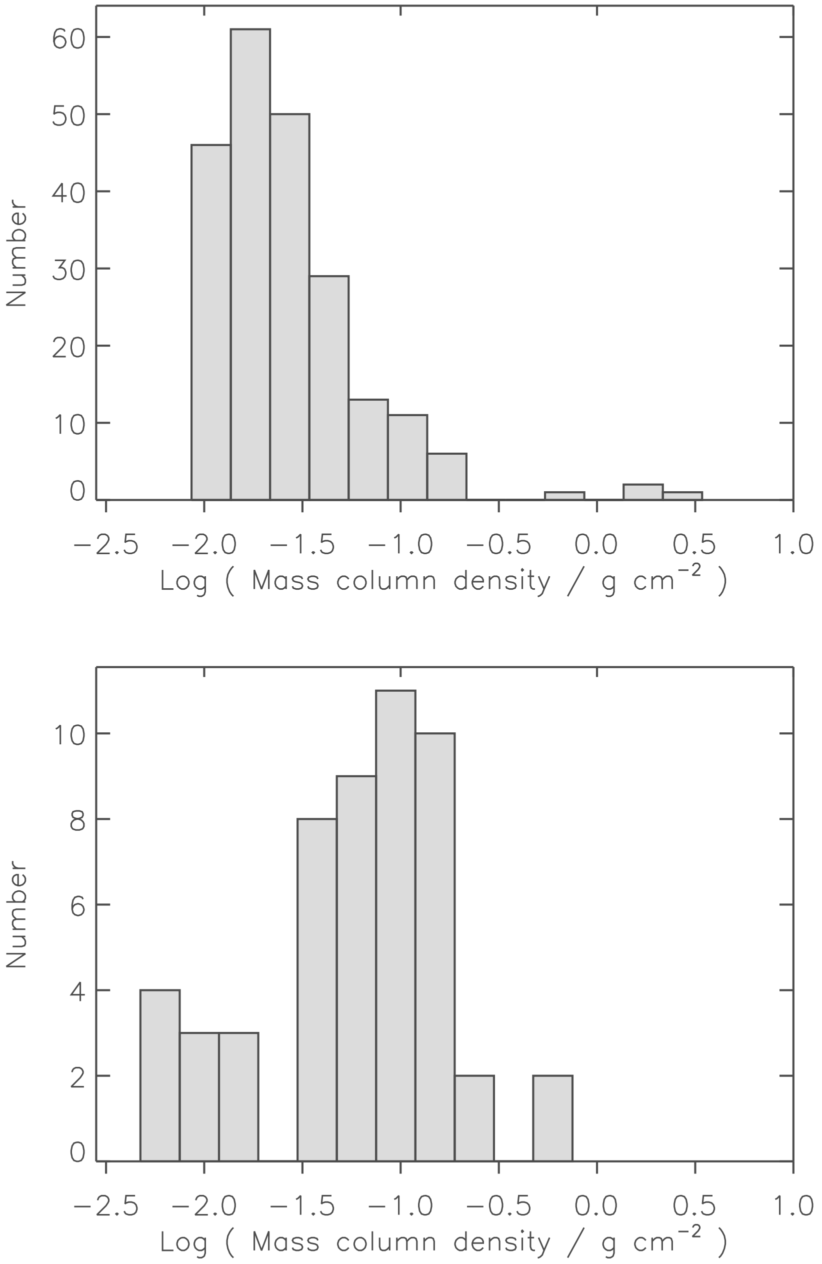

Fig. 22.— Top: histogram of the 220 mass column densities for the HDL (Moore et al. 2007). Bottom: histogram of the SCUBA Legacy mass column densities for KR 7, KR 81, and KR 120 from Table 3 and for KR 140 from Kerton et al. (2001). The bin size is 0.2 dex.

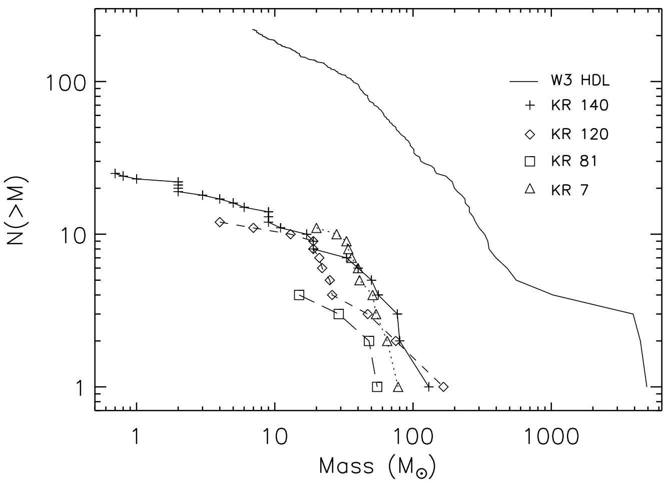

Fig. 23.— Cumulative plot of sub-mm source mass for the HDL (solid line, from Moore et al. 2007), KR 7 (triangles), KR 81 (squares), KR 120 (diamonds), and KR 140 (crosses, from Kerton et al. 2001).

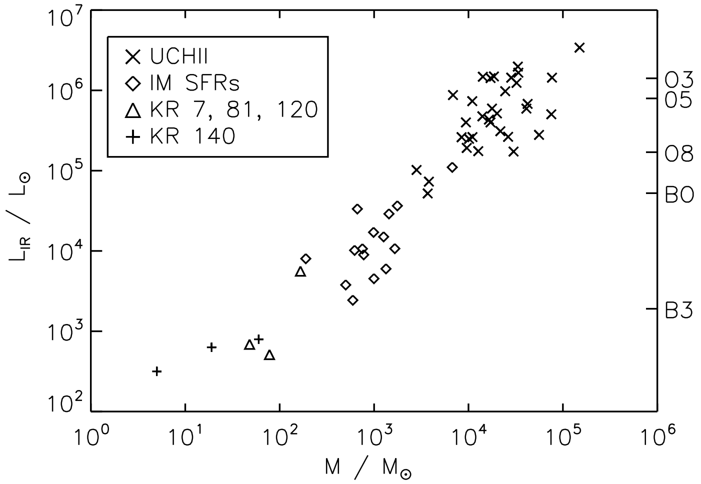

Fig. 24.— Luminosity vs. associated mass. IM SFRs (15 objects) are diamonds, and UCH II regions (33 objects) are crosses (from Arvidsson et al. 2010). The three prominent KR sub-mm sources are triangles. KR 140 sources are taken from Kerton et al. (2001). The scale on the right is spectral type of a single class V star.